

## Growth and characterization of PbSe and $\text{Pb}_{1-x}\text{Sn}_x\text{Se}$ on Si (100)

H. K. Sachar,<sup>a)</sup> I. Chao, P. J. McCann,<sup>b)</sup> and X. M. Fang

*School of Electrical and Computer Engineering and Laboratory for Electronic Properties of Materials, University of Oklahoma, Norman, Oklahoma 73019*

(Received 11 September 1998; accepted for publication 2 February 1999)

PbSe and  $\text{Pb}_{1-x}\text{Sn}_x\text{Se}$  layers, with thicknesses ranging from 1 to 5  $\mu\text{m}$ , were grown by liquid phase epitaxy on Si (100) substrates using PbSe/BaF<sub>2</sub>/CaF<sub>2</sub> buffer layers grown by molecular beam epitaxy. Optical Nomarski characterization revealed excellent surface morphologies and good growth solution wipeoffs. Although most PbSe layers were free of cracks over the entire 8  $\times$  8 mm<sup>2</sup> substrate area, ternary  $\text{Pb}_{1-x}\text{Sn}_x\text{Se}$  layers exhibited varying crack densities ranging from zero in the center of samples to over 30 cracks/cm at the edges. High resolution x-ray diffraction (HRXRD) measurements of crack-free PbSe layers showed a residual in-plane tensile strain of 0.21% indicating that most of the 0.74% thermal expansion mismatch strain was absorbed by plastic deformation. HRXRD full width half maxima values of less than 200 arc sec showed that these layers also had high crystalline quality. Fourier transform infrared transmission measurements at room temperature and 110 K showed absorption edges in the range of 270–80 meV, depending on temperature and tin content. This work shows that these materials should be suitable for fabrication of mid-infrared devices covering the 4.6–16  $\mu\text{m}$  spectral range. © 1999 American Institute of Physics. [S0021-8979(99)00510-1]

### I. INTRODUCTION

The study of IV–VI semiconductors such as PbSe and  $\text{Pb}_{1-x}\text{Sn}_x\text{Se}$  has been motivated by their use as mid-infrared laser materials. Growth of these materials on Si substrates is advantageous because silicon substrates are available in large dimensions and are considerably less expensive than conventionally used IV–VI substrates. High quality layers of PbSe, PbTe, and  $\text{Pb}_{1-x}\text{Sn}_x\text{Se}$  have been grown heteroepitaxially on Si (111) substrates using group IIa fluoride insulators as buffer layers.<sup>1–3</sup> The growth of these IV–VI layers on Si (111) substrates has allowed fabrication of monolithic infrared detector arrays in which infrared detection is performed in the IV–VI semiconductor layer and signal processing can be performed in the Si wafer. Device fabrication requirements for IV–VI lasers, however, favor growth on (100)-oriented substrates since IV–VI materials cleave preferentially along their {100} planes and this allows formation of in-plane cleaved Fabry–Perot cavities. If IV–VI materials are grown on (100)-oriented Si substrates cleavage problems persist due to the tendency of Si to cleave along the {111} planes, but this problem can be solved by lifting off the IV–VI epilayer from the Si substrate through selective etching of a molecular beam epitaxially (MBE) grown BaF<sub>2</sub> buffer layer.<sup>4</sup> With a minimum of thermally resistive IV–VI materials, IV–VI lasers fabricated in this manner should have continuous wave operating temperatures greater than 260 K, within the range of thermoelectric cooling modules.<sup>5</sup>

The large thermal expansion coefficient mismatch between IV–VI semiconductors and silicon results in significant tensile strain when structures are cooled following

growth at high temperatures. MBE growth of PbSe on Si (100) at 280 °C on BaF<sub>2</sub>/CaF<sub>2</sub> buffer layers results in high crack density because of this strain.<sup>6</sup> Interestingly, crack-free layers of PbSe can be obtained by liquid phase epitaxy (LPE) growth on the MBE-grown structures.<sup>7</sup> These layers were free of cracks and metal inclusions over an 8  $\times$  8 mm<sup>2</sup> area and exhibited excellent growth solution wipeoff with no melt adhesions. Growth of crack-free PbSe layers on Si (100) by LPE is especially remarkable considering the fact that LPE growth temperatures are almost 200° higher than MBE growth temperatures and are thus subject to much more thermal strain. Ternary  $\text{Pb}_{1-x}\text{Sn}_x\text{Se}$  has a smaller band gap and larger refractive index than PbSe, so it can be used as the active layer in heterostructure lasers. In this study, LPE experiments have been extended to  $\text{Pb}_{1-x}\text{Sn}_x\text{Se}$  growth on Si (100) substrates using similar MBE-grown PbSe/BaF<sub>2</sub>/CaF<sub>2</sub> buffer layers as the earlier work.

### II. EXPERIMENTAL PROCEDURE

PbSe and  $\text{Pb}_{1-x}\text{Sn}_x\text{Se}$  layers were grown by LPE from Pb-rich  $(\text{Pb}_{1-x_1}\text{Sn}_{x_1})_{1-z}\text{Se}_z$  liquid solutions on PbSe/BaF<sub>2</sub>/CaF<sub>2</sub>/Si (100) structures prepared by MBE. The MBE growth procedures for the buffer layer structures are described by Strecker *et al.*<sup>7</sup> LPE growth employed liquid solutions prepared by combining weighed amounts of Pb, PbSe, and Sn according to relations derived from the molecular weights of the respective constituents. Based on previously published phase equilibria data for  $(\text{Pb}_{1-x_1}\text{Sn}_{x_1})_{1-z}\text{Se}_z$ ,<sup>8</sup> the selenium concentration,  $z$ , was chosen to be 0.25 at. % giving a nucleation temperature of about 470 °C for growth of a Pb<sub>0.95</sub>Sn<sub>0.05</sub>Se layer. Tin concentrations,  $x_1$ , in the liquid growth solutions for different ternary layers were equal to 3%, 5%, 6%, 7%, 9%, 10%, and

<sup>a)</sup>Present address: Micron Technologies, Inc., Boise, ID.

<sup>b)</sup>Electronic mail: pmccann@ou.edu

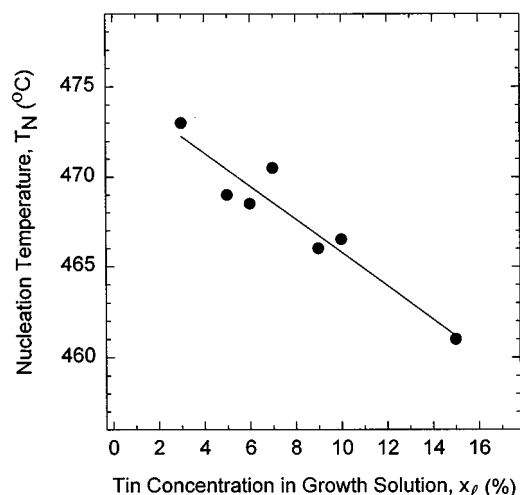


FIG. 1. Nucleation temperature vs percentage tin in  $(Pb_{1-x_l}Sn_{x_l})_{0.9975}Se_{0.0025}$  solutions. Liquid phase epitaxy was used to grow pseudobinary  $Pb_{1-x}Sn_x$ Se layers on Si (100) substrates from these solutions.

15%. The melt constituents were loaded into one of the wells of a graphite boat, and the temperature of the furnace was increased to 650 °C and maintained for about 1 h to allow growth solution homogenization. The furnace temperature was then reduced to about 30° above the expected nucleation temperature. The melt surface was observed with an optical microscope while reducing the furnace temperature at a rate of 2 °C/min. The temperature at which nucleation was observed on the melt surface was recorded. The furnace was then cooled back to room temperature and the silicon substrate with the MBE-grown PbSe/BaF<sub>2</sub>/CaF<sub>2</sub> buffer layer was placed in the recess provided on the graphite slider. The furnace temperature was kept below 500 °C in order to minimize the thermal stress to which the MBE-grown PbSe layer was subjected. A controlled cooling ramp of 2 °C/min was initiated and the graphite slider was pulled to position the substrate under the growth solution well at about 2°–3° above the measured nucleation temperature. After 80° of cooling, the slider was pulled to position the substrate away from the melt thereby terminating growth.

Optical Nomarski microscopy was used to study the surfaces of the LPE-grown PbSe and  $Pb_{1-x}Sn_x$ Se layers. Defects including metal inclusions and cracks in the IV–VI

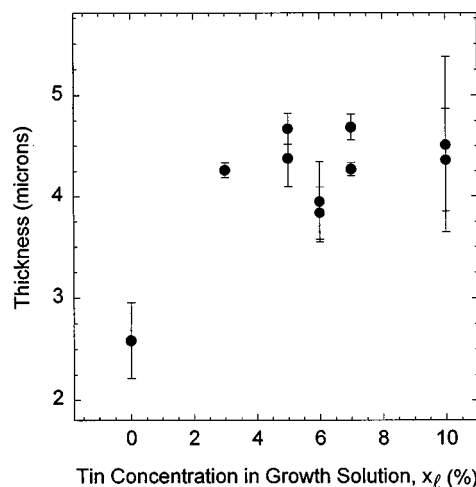


FIG. 2. Thicknesses of LPE-grown layers vs percentage tin in the liquid growth solution for 40 min of growth during cooling from about 470 to 390 °C. Thicknesses of ternary  $Pb_{1-x}Sn_x$ Se layers are almost twice that of binary PbSe layers. The percentage Se,  $z$ , for the PbSe layers was 0.20%, while  $z$  for the ternary layers was 0.25%. Thicknesses from two different samples are shown for ternary layers with 5%, 6%, 7%, and 10% tin in the liquid growth solution. The error bars indicate the range in thickness values obtained for different step profile scans.

semiconductor layers were easily observable in areas measuring  $1.01 \times 0.76 \text{ mm}^2$ . Layer thicknesses were measured using a Tencor step scan profiler. Lattice parameters and crystalline quality of the layers were measured using a Philips Materials Research high resolution x-ray diffraction (HRXRD) system with a four-bounce monochromator. Infrared transmission through the PbSe and  $Pb_xSn_x$ Se layers at room temperature and at liquid nitrogen-cooled temperatures was measured using a vacuum bench Bruker IR/98 Fourier transform infrared (FTIR) spectrometer equipped with a Hg<sub>1-x</sub>Cd<sub>x</sub>Te detector having a peak detectivity of 16 μm.

### III. RESULTS AND DISCUSSION

Figure 1 shows a plot of measured nucleation temperatures for  $(Pb_{1-x_l}Sn_{x_l})_{1-z}Se_z$  growth solutions versus percentage tin,  $x_l$ , in the liquid growth solution. As evident from the plot, the nucleation temperature decreases as the percentage tin increases. This is consistent with the eutectic nature of the Pb–Sn–Se phase diagram for mixtures near the Pb corner. Figure 2 shows a plot of thickness of the LPE-

TABLE I. MBE layer thicknesses, LPE layer compositions and thicknesses, and surface morphologies of the structures grown for this study.

| Sample No. | MBE layer thicknesses |                       |           | Pb <sub>1-x</sub> Sn <sub>x</sub> Se LPE layers |                |                              |
|------------|-----------------------|-----------------------|-----------|---|----------------|------------------------------|
|            | CaF <sub>2</sub> (μm) | BaF <sub>2</sub> (μm) | PbSe (μm) | Tin, $x$ (%)                                    | Thickness (μm) | Surface                      |
| W113-H9    | 0.02                  | 0.47                  | 0.1       | 0.0   | 2.2            | Crack-free                   |
| W113-H15   | 0.02                  | 0.47                  | 0.1       | 6.0   | 3.8            | $\langle 100 \rangle$ Cracks |
| W222-H12   | 0.04                  | 0.47                  | 2.2       | 5.0   | 4.7            | $\langle 100 \rangle$ Cracks |
| W222-H13   | 0.04                  | 0.47                  | 2.2       | 3.0   | 4.3            | $\langle 100 \rangle$ Cracks |
| W222-H14   | 0.04                  | 0.47                  | 2.2       | 7.0   | 4.7            | $\langle 100 \rangle$ Cracks |
| W222-H20   | 0.04                  | 0.47                  | 2.2       | 5.0   | 4.4            | $\langle 100 \rangle$ Cracks |
| W245-H17   | 0.06                  | 0.90                  | 0.8       | 10  | 4.5            | Many cracks                  |

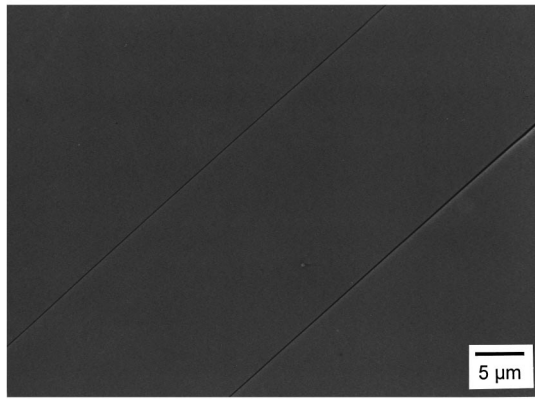


FIG. 3. Scanning electron micrograph showing the surface of a LPE-grown  $\text{Pb}_{0.95}\text{Sn}_{0.05}\text{Se}$  layer (W222-H20). Two parallel cracks along the  $[100]$  direction are observed in the micrograph.

grown layers versus percentage tin in the liquid growth solution. The thicknesses of the ternary layers are almost twice the thicknesses of binary PbSe layers grown for the same duration of 40 min ( $80^\circ$  of cooling). This could be due to faster Se diffusion through the predominantly Pb–Sn liquid solution.

Table I lists the respective MBE-grown and LPE-grown layer properties for each sample prepared for this study. Unlike binary PbSe layers grown by LPE on Si (100) substrates using  $\text{PbSe}/\text{BaF}_2/\text{CaF}_2$  buffer layers,  $\text{Pb}_{1-x}\text{Sn}_x\text{Se}$  layers grown by LPE using similar buffer layer structures were not crack free. Figure 3 shows a scanning electron micrograph of the growth surface of a LPE-grown  $\text{Pb}_{0.95}\text{Sn}_{0.05}\text{Se}$  layer. Two parallel cracks along the  $[100]$  direction are observed in the micrograph. The line density for cracks in this  $\text{Pb}_{0.95}\text{Sn}_{0.05}\text{Se}$  layer varied from 0 to about 30 cracks/cm yielding an average line density of approximately 12 cracks/cm over a typical distance of 7 mm. This value is still much lower than the  $10^3 \text{ cm}^{-1}$  line density for cracks observed in MBE-grown PbSe layers on Si (100).<sup>7</sup> The distribution of cracks over a  $42 \text{ mm}^2$  area is shown in Fig. 4. Note that a large area in the center of the sample is crack free, while the perimeter of the sample contains most of the cracks. A crack-free center region can be due to plastic deformation via movement of

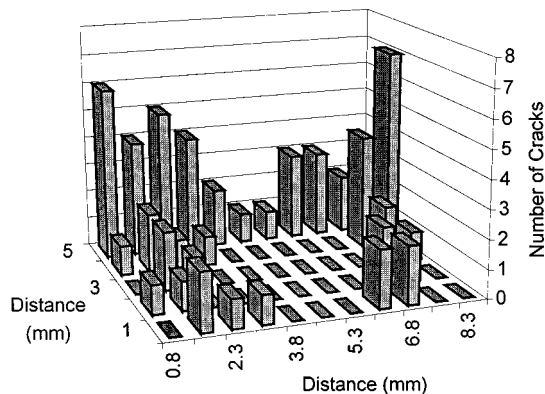


FIG. 4. Distribution of cracks over a  $42 \text{ mm}^2$  area of a  $\text{Pb}_{0.95}\text{Sn}_{0.05}\text{Se}$  layer (W222-H20). Each bar indicates the number of cracks observed in an area measuring  $1.01 \times 0.76 \text{ mm}^2$ .

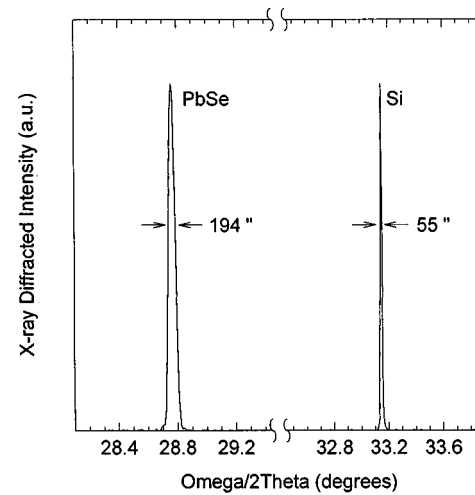


FIG. 5. Symmetric (004)  $\Omega/2\theta$  scan for a LPE-grown PbSe layer (W113-H9) showing a PbSe peak along with a Si peak and their respective FWHM values.

dislocations along the secondary  $\langle 001 \rangle \{110\}$  glide system in IV–VI compounds,<sup>9</sup> while the cracks around the perimeter can be due to higher strain fields caused by entanglement of these gliding dislocations.

A symmetric (004)  $\Omega/2\theta$  HRXRD scan containing peaks for silicon and PbSe is shown in Fig. 5. These data were used to calculate the residual strain in the LPE-grown PbSe layers. Residual strain in the growth direction,  $\epsilon_{\perp}$ , is given by  $(a_{\perp} - a_0)/a_0$  where  $a_{\perp}$  is the measured lattice parameter of the strained layer in the growth direction and  $a_0$  is the unstrained lattice parameter,  $6.126 \text{ \AA}$ . The lattice parameter normal to the substrate for a binary PbSe layer was determined by HRXRD to be  $6.122 \text{ \AA}$ , yielding a compressive strain value of  $\epsilon_{\perp} = -0.065\%$ . Using the elastic constants for PbSe,<sup>10</sup> the tensile strain parallel to the substrate was calculated to be  $0.21\%$ . If no plastic deformation were allowed on cooling down from growth to room temperature, the LPE-grown PbSe layers would be subject to an in-plane tensile strain of  $0.74\%$ . This analysis shows that about  $72\%$  of the thermal expansion mismatch strain is absorbed by plastic deformation of the PbSe layer. In spite of such large plastic deformation, the crystalline quality of the PbSe layer is good as indicated by typical HRXRD full width half maxima (FWHM) values below  $200$  arc sec.

FTIR transmission spectra for a binary PbSe layer obtained at room temperature and low temperature ( $125 \text{ K}$ ) are shown in Fig. 6. Absorption edges around  $4.6$  and  $6.5 \mu\text{m}$ , respectively, are evident from the spectra. Figure 7 shows the FTIR transmission spectra for a  $\text{Pb}_{0.95}\text{Sn}_{0.05}\text{Se}$  layer obtained at room temperature and low temperature ( $111 \text{ K}$ ). Absorption edges around  $5.6$  and  $9.2 \mu\text{m}$ , respectively, are evident from these spectra. The room temperature and low temperature ( $116 \text{ K}$ ) FTIR spectra for a  $\text{Pb}_{0.92}\text{Sn}_{0.08}\text{Se}$  layer grown from a  $(\text{Pb}_{0.90}\text{Sn}_{0.10})_{0.9975}\text{Se}_{0.0025}$  solution are shown in Fig. 8. Absorption edges around  $6.9$  and  $15.4 \mu\text{m}$ , respectively, are evident from these spectra. Note that all spectra show below band gap Fabry–Perot interference fringes. Figure 9 is a plot of absorption edge energies versus percentage tin in the liquid growth solution for the  $\text{Pb}_{1-x}\text{Sn}_x\text{Se}$  layers shown

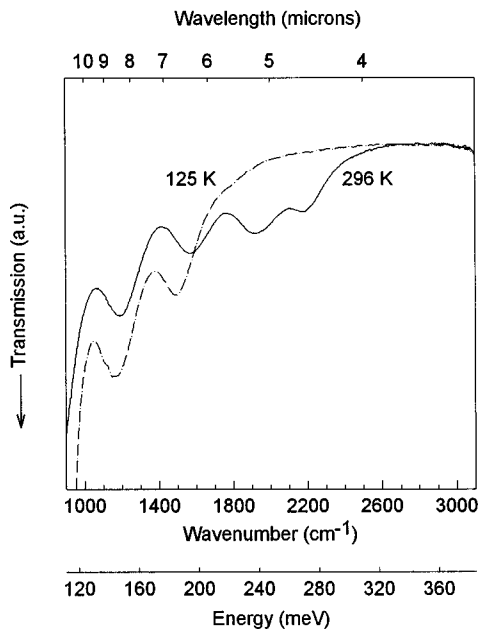


FIG. 6. FTIR transmission spectra for a binary PbSe layer (W113-H9) at room temperature and 125 K.

in Figs. 6–8 as well as the other  $Pb_{1-x}Sn_xSe$  layers grown for this study. These FTIR absorption edge data, which cover the 4.6–16  $\mu m$  spectral range for tin contents of 0%–10%, respectively, agree very well with emission energy data for IV–VI lasers fabricated from  $Pb_{1-x}Sn_xSe$  alloys having similar compositions.<sup>11</sup>

Figure 10 shows room temperature FTIR transmission data for PbSe and  $Pb_{0.95}Sn_{0.05}Se$  layers before and after cryogenic temperature cycling down to about 110 K. Both mate-

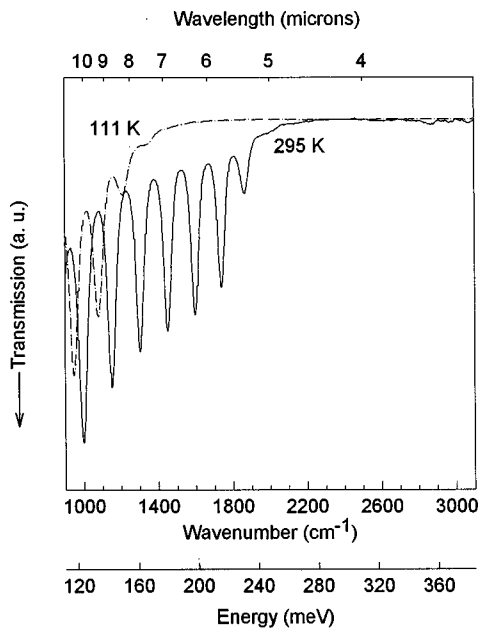


FIG. 7. FTIR transmission spectra for a  $Pb_{0.95}Sn_{0.05}Se$  layer (W222-H12) grown from a  $(Pb_{0.95}Sn_{0.05})_{0.9975}Se_{0.0025}$  solution at room temperature and 111 K. Note the shift of absorption edges to lower energies and the more closely spaced Fabry–Perot interference fringes, indicating a thicker layer, as compared to the data in Fig. 6.

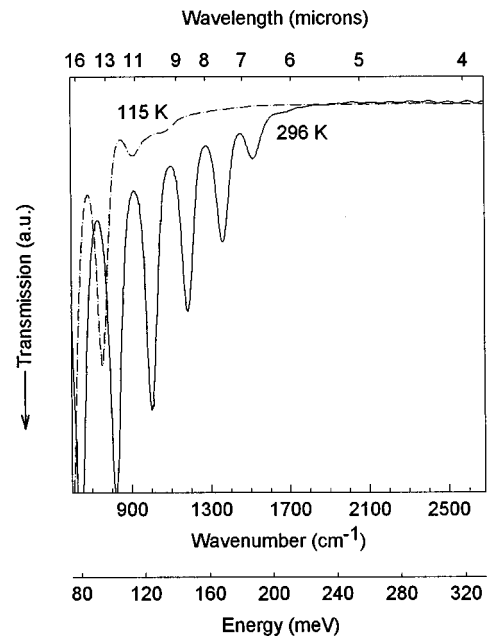


FIG. 8. FTIR transmission spectra for a  $Pb_{0.92}Sn_{0.08}Se$  layer (W245-H17) grown from a  $(Pb_{0.90}Sn_{0.10})_{0.9975}Se_{0.0025}$  solution at room temperature and 116 K. Note again the additional shift of absorption edges to lower energies.

rials show absorption edge shifts to lower energies of about 50 and 160  $cm^{-1}$ , respectively. These shifts are most certainly caused by relaxation of residual strain associated with crack formation due to the thermal stress at cryogenic temperatures.<sup>7</sup> HRXRD measurements of these cracked PbSe layers, in fact, yield a lattice parameter of 6.126 Å, showing complete relaxation of as-grown tensile strain. These measurements also showed an increased FWHM value of 238 arc sec indicating that the thermal expansion mismatch strain at 110 K caused crystalline quality degradation. Using the relationship between change in strain and change in band gap energy for (100)-oriented PbTe layers derived from elastic moduli and deformation potential values,<sup>12</sup>

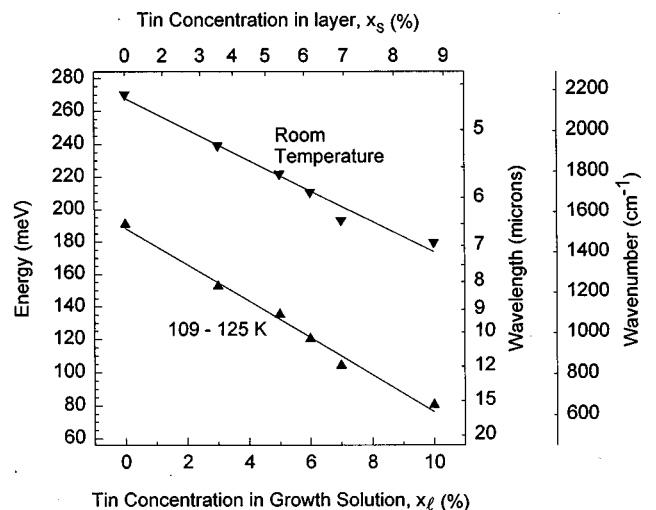


FIG. 9. Absorption edge energy vs percentage tin for  $Pb_{1-x}Sn_xSe$  layers with 0%, 3%, 5%, 6%, 7%, and 10% tin in the liquid growth solution. The percentage tin in the solid layer, obtained from previously measured phase equilibria data (see Ref. 8), is indicated on the top scale.

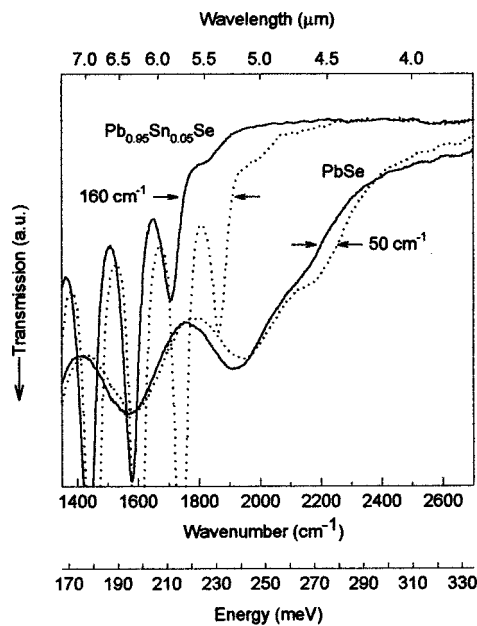


FIG. 10. Room temperature FTIR transmission spectra for a PbSe and a  $\text{Pb}_{0.95}\text{Sn}_{0.05}\text{Se}$  layer before (dotted lines) and after (solid lines) cryogenic cooling to  $\sim 110$  K. Thermal expansion mismatch at low temperature causes the layers to crack, thereby relieving the residual as-grown epitaxial layer strain. The solid lines represent the transmission spectra for unstrained layers, while the dotted lines represent transmission spectra for the as-grown strained layers. Note the much larger absorption edge shift for the ternary  $\text{Pb}_{0.95}\text{Sn}_{0.05}\text{Se}$  layer indicating a larger as-grown strain.

$$\Delta\epsilon_{\parallel} = 0.312\Delta E_g (\text{eV}), \quad (1)$$

a change in strain of 0.19% for the 6.2 meV ( $50 \text{ cm}^{-1}$ ) absorption edge shift for PbSe is obtained. (Reliable deformation potential values for PbSe could not be found, so the expression for PbTe is used here.) This value is in excellent agreement with the 0.21% value obtained from HRXRD measurements.

Using Eq. (1) and assuming that additional crack formation due to cryogenic cycling causes complete strain relaxation, an as-grown strain of 0.62% is obtained for the  $\text{Pb}_{0.95}\text{Sn}_{0.05}\text{Se}$  layer, which exhibits a 19.9 meV ( $160 \text{ cm}^{-1}$ ) absorption edge shift. This strain is  $3\times$  larger than the as-grown residual strain in PbSe and within 84% of the strain value if no plastic deformation occurred. With only about 16% of the thermal expansion mismatch strain being absorbed by plastic deformation, it is reasonable to expect crack formation to become an additional strain relief mechanism in the  $\text{Pb}_{0.95}\text{Sn}_{0.05}\text{Se}$  layer. Greater  $\text{Pb}_{1-x}\text{Sn}_x\text{Se}$  layer thickness, 4.7 versus  $2.2 \mu\text{m}$  for a crack-free PbSe layer grown on the same MBE-grown buffer layer structure, could be the cause of cracking in these ternary alloy layers. However, the much larger strain experienced by the  $\text{Pb}_{0.95}\text{Sn}_{0.05}\text{Se}$  layer, which includes the strain relieved by cracking plus the  $3\times$  larger residual strain, suggests that there is a significant solid solution hardening effect in  $\text{Pb}_{1-x}\text{Sn}_x\text{Se}$  ternary alloys. Figure 11 is a plot of calculated refractive indices versus energy at room temperature for  $\text{Pb}_{1-x}\text{Sn}_x\text{Se}$  layers grown with 3%, 5%, and 10% tin in the growth solution. These data were obtained from FTIR transmission measurements using the relation<sup>13</sup>

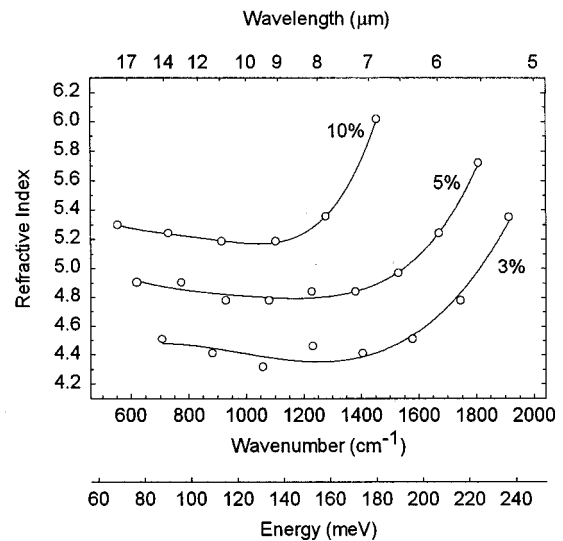


FIG. 11. Room temperature index of refraction data for  $\text{Pb}_{1-x}\text{Sn}_x\text{Se}$  layers grown from liquid solutions having 3%, 5%, and 10% tin. These data are calculated from FTIR transmission Fabry–Perot interference fringe spacing and measured epitaxial layer thicknesses.

$$n = \frac{1}{2\Delta\nu t}, \quad (2)$$

where  $\Delta\nu$  is the spacing between Fabry–Perot interference fringes and  $t$  is the thickness of the LPE-grown layer plus the thickness of the MBE-grown PbSe layer. This method, although somewhat imprecise because a constant index of refraction is assumed throughout the composite LPE/MBE  $\text{Pb}_{1-x}\text{Sn}_x\text{Se}/\text{PbSe}$  structure, yields refractive index values within 10% of values published for bulk  $\text{Pb}_{1-x}\text{Sn}_x\text{Se}$  alloys with similar compositions.<sup>14</sup> As expected, and as required for heterostructure laser design, layers with higher tin content, i.e., smaller band gap, have larger refractive indices. These data also show the expected increase in refractive index values as photon energy approaches the band gap energy. In addition, room temperature refractive index values did not change significantly with epitaxial layer strain relaxation. This can be seen in the FTIR transmission spectrum for the  $\text{Pb}_{0.95}\text{Sn}_{0.05}\text{Se}$  layer in Fig. 10, which shows a significant change in absorption edge, but no change in Fabry–Perot interference fringe spacing. So although strain can cause a significant band gap energy shift, it does not cause a refractive index shift.

#### IV. CONCLUSIONS

PbSe and  $\text{Pb}_{1-x}\text{Sn}_x\text{Se}$  layers exhibiting smooth surface morphologies and complete growth solution wipeoffs were grown by LPE on Si (100) substrates using MBE-grown PbSe/BaF<sub>2</sub>/CaF<sub>2</sub> buffer layer structures. Binary PbSe layers were crack free and exhibited good crystallinity with HRXRD FWHM values below 200 arc sec. While ternary  $\text{Pb}_x\text{Sn}_x\text{Se}$  layers were not entirely crack free, large regions in the center of the samples were, and this may allow use of these LPE-grown materials for device fabrication. FTIR transmission spectra at room temperature and 110 K showed absorption edges in the range of 270–80 meV, depending on

temperature and tin content, suggesting that these materials should be suitable for fabrication of mid-infrared devices covering the 4.6–16  $\mu\text{m}$  spectral range. Residual strain values for as-grown binary PbSe layers were in the range of 0.2% as determined by both HRXRD lattice parameter and FTIR absorption edge shift measurements. The FTIR determined strain value for an as-grown  $\text{Pb}_{0.95}\text{Sn}_{0.05}\text{Se}$  layer was in the range of 0.6%. This  $3\times$  larger value indicates that alloying with tin causes a solid solution hardening effect in ternary  $\text{Pb}_{1-x}\text{Sn}_x\text{Se}$  layers. Refractive index values for  $\text{Pb}_{1-x}\text{Sn}_x\text{Se}$  layers were also obtained from FTIR transmission spectra, and no change was observed with relaxation of as-grown strain.

## ACKNOWLEDGMENTS

The authors thank the National Science Foundation, the National Aeronautics and Space Administration, and the Oklahoma Center for Advancement of Science and Technology, Grant Nos. DMR-9416871, NGT-30308, and AR6-054, respectively, for financial support.

- <sup>1</sup>H. Zogg and M. Hüppi, *Appl. Phys. Lett.* **47**, 133 (1985).
- <sup>2</sup>C. Maissen, J. Masek, H. Zogg, and S. Blunier, *Appl. Phys. Lett.* **53**, 1608 (1988).
- <sup>3</sup>H. Zogg, C. Maissen, J. Masek, S. Blunier, A. Lambrecht, and M. Tacke, *Appl. Phys. Lett.* **55**, 969 (1989).
- <sup>4</sup>H. Wu, X. M. Fang, R. Salas, D. McAlister, and P. J. McCann, *Thin Solid Films* (submitted).
- <sup>5</sup>K. R. Lewelling and P. J. McCann, *IEEE Photonics Technol. Lett.* **9**, 297 (1997).
- <sup>6</sup>P. Muller, A. Fach, J. John, A. N. Tiwari, H. Zogg, and G. Kistorz, *J. Appl. Phys.* **79**, 1911 (1996).
- <sup>7</sup>B. S. Strecker, P. J. McCann, X. M. Fang, R. J. Hauenstein, M. O'Steen, and M. B. Johnson, *J. Electron. Mater.* **26**, 444 (1997).
- <sup>8</sup>P. J. McCann, J. Fuchs, Z. Feit, and C. G. Fonstad, *J. Appl. Phys.* **62**, 2994 (1987).
- <sup>9</sup>A. Kelly, *Strong Solids* (Oxford University Press, London, 1966), p. 202.
- <sup>10</sup>*Semiconductors Other than Group IV and III-V Compounds*, edited by O. Madelung (Springer, Berlin, 1992), p. 44.
- <sup>11</sup>T. C. Harmon, A. R. Calawa, I. Melngailis, and J. O. Dimmock, *Appl. Phys. Lett.* **14**, 333 (1969).
- <sup>12</sup>J. W. Tomm, L. Werner, D. Genzow, K. Herrmann, D. Schikora, and J. Griesche, *Phys. Status Solidi A* **106**, 509 (1988).
- <sup>13</sup>P. J. McCann, L. Li, and J. E. Furneaux, *Narrow Gap Semiconductors 1995* (Institute of Physics, London, 1995), p. 150.
- <sup>14</sup>P. K. Cheo, *Handbook of Solid State Lasers* (Marcel Dekker, New York, 1989), p. 227.